Unveiling Liquid-Crystalline Lipids in the Urothelial Membrane through Cryo-EM

Authors: Haruaki Yanagisawa[1], Yoshihiro Kita[2,3], Toshiyuki Oda[4*], and Masahide Kikkawa[1*]

Affiliations:

[1] Department of Cell Biology and Anatomy, Graduate School of Medicine, The University of Tokyo, 7-3-1 Hongo, Bunkyo-ku, Tokyo, 113-0033, Japan,

[2] Life Sciences Core Facility, Graduate School of Medicine, The University of Tokyo, 7-3-1 Hongo, Bunkyo-ku, Tokyo 113-0033, Japan,

[3] Department of Lipidomics, Graduate School of Medicine, The University of Tokyo, 7-3-1 Hongo, Bunkyo-ku, Tokyo 113-0033, Japan.

[4] Department of Anatomy and Structural Biology, Graduate School of Medicine, University of Yamanashi, 1110 Shimokato, Chuo, Yamanashi, 409-3898, Japan.

*Correspondence to: toda@yamanashi.ac.jp, mkikkawa@m.u-tokyo.ac.jp

Abstract

The urothelium, a distinct epithelial tissue lining the urinary tract, serves as an essential component in preserving urinary tract integrity and thwarting infections. The asymmetric unit membrane (AUM), primarily composed of the uroplakin complex, constitutes a critical permeability barrier in fulfilling this role. However, the molecular architectures of both the AUM and the uroplakin complex have remained enigmatic due to the paucity of high-resolution structural data. In this study, we utilized cryo-electron microscopy to elucidate the three-dimensional structure of the uroplakin complex within the porcine AUM. While the global resolution achieved was 3.5 Å, we acknowledge that due to orientation bias, the resolution in the vertical direction was determined to be 6.3 Å. Our findings unveiled that the uroplakin complexes are situated within hexagonally arranged crystalline lipid membrane domains, rich in hexosylceramides. Moreover, our research rectifies a misconception in a previous model by confirming the existence of a domain initially believed to be absent, and pinpointing the accurate location of a crucial *Escherichia coli* binding site implicated in urinary tract infections. These discoveries offer valuable insights into the molecular underpinnings governing the permeability barrier function of the urothelium and the orchestrated lipid phase formation within the plasma membrane.

Introduction

The urothelium, which lines the urinary tract, performs a dual function: it serves as a permeability barrier, effectively preventing the leakage of urine components into surrounding tissue while undergoing morphological changes to adapt to the distention and contraction that occurs during the micturition cycle (Deng et al., 2001; Wu et al., 2009; Apodaca, 2004; Khandelwal et al., 2009). The apical surface of the urothelium is covered by numerous structurally rigid membrane plaques, known as asymmetric unit membranes (AUM), as observed by electron microscopy (Hicks, 1965; Hu et al., 2000; Jenkins and Woolf, 2007). The AUMs are composed of hexagonally arranged 16-nm uroplakin complexes containing four major proteins, UPIa, UPIb, UPII, and UPIIIa (Lee, 2011). UPIa and UPIb have four transmembrane domains and belong to the tetraspanin family (Yu et al., 1994). Meanwhile, UPII and UPIIIa each possess a single transmembrane domain and form Ia/II and Ib/IIIa heterodimers within the endoplasmic reticulum (ER) in conjunction with UPIa and UPIb, respectively (Hu et al., 2005; Tu et al., 2002). In the post-Golgi compartment, UP heterodimers are assembled into paracrystalline arrays (Liang et al., 2001). The AUM's quasi-crystalline symmetry has been leveraged in the structural investigation of the uroplakin complex, as documented by several studies (Min et al., 2006; Min et al., 2003; Min et al., 2002; Walz et al., 1995; Zhou et al., 2001). While cryo-electron microscopy of tannic-acid-stained AUM has enabled the identification of the orientation of transmembrane helices in tetraspanin pairs (Min et al., 2006; Wang et al., 2009), the resolution of the resulting electron density map remains insufficient for a comprehensive study of the secondary structures of the extracellular domains or for the localization of individual UP subunits.

The uroplakin complex also plays a crucial role in the development of urinary tract infections, as it facilitates *Escherichia coli's* attachment to the urothelium (Hultgren et al., 1993; Hooton and Stamm, 1997). This attachment is facilitated by the interaction between the N-glycosylated

66 UPIa's mannose residues and the FimH lectin located at the tip of the bacterium's pili (Zhou
67 et al., 2001). The binding of FimH to UPIa triggers phosphorylation of UPIIIa and subsequent
68 apoptosis of the urothelial cells (Thumbikat et al., 2009). Furthermore, it has been postulated
69 that this FimH-UPIa interaction induces conformational alterations in the transmembrane helix
70 bundles (Wang et al., 2009). However, it is unclear whether FimH's binding to a flexible
71 carbohydrate chain can change the conformation of a rigid uroplakin complex. In addition, the
72 positioning of the heterodimer has been inferred by comparing the uroplakin structure with and
73 without bound FimH (Min et al., 2002). Nevertheless, the low resolution of the electron density
74 map hinders the validity of these conclusions.
75 In this study, we reconstructed the 3D structure of the uroplakin complex by observing tilted
76 AUMs using cryo-electron microscopy. By combining random conical tilt and single particle
77 analysis (Sorzano et al., 2015; Frank et al., 1978; Righetto et al., 2019; Radermacher, 1988),
78 we were able to build an accurate model of the uroplakin hexameric complex.
79
80 **Results**
81
82 *Cryo-Electron Microscopy of AUM*
83 To determine the high-resolution structure of the uroplakin complex, we isolated the AUM
84 from porcine urinary bladders, leveraging its resistance to sarkosyl (Liang et al., 1999), and
85 employed cryo-electron microscopy techniques. Initially, we used cryo-electron tomography
86 to observe the AUM; however, the obtained structure was of low resolution as a result of the
87 irradiation-induced distortion of the specimen (Oda et al., 2022; Dutka et al., 2023).
88 Subsequently, we performed single particle analysis on AUM samples tilted up to 55° (Figures
89 1A and 1B), resulting in a global resolution of 3.5 Å, with 3.2 Å and 6.3 Å resolutions in the
90 transverse and vertical directions, respectively (Figures 1C, 1D, and S1B). These resolutions

allowed us to construct a model of the main chains and some side chains, based on AlphaFold predictions, with the exceptions of the 90-101 loop of UPII and the cytoplasmic loop of UPIIIa due to their flexibility (Jumper et al., 2021) (Figure 2).

To our surprise, we found that the hexagonally arranged liquid-crystalline lipids were not only within the central pore but also in the inter-complex regions, spanning the entire outer leaflet of the AUM (Figure 1D, 2A, Movie S1). The crystalline lipids were tightly packed, with a distance of ~4.8 Å between them (Zhao et al., 2021; Ghysels et al., 2019). Further local refinement focusing on the extracellular domain revealed the additional outermost part of the lipid densities, suggesting a structural heterogeneity in the association between the lipids and the uroplakin complex (Figure S1A). Although the head groups of most lipids were unresolved due to the insufficient vertical resolution and the random orientations, densities of some lipids were continuous with those of the side chains, suggesting possible interactions (Figure 2C). Some lipids appeared to be stabilized by vertically-aligned bulky side chains (Figure 3) (Ulmschneider and Sansom, 2001). Although the majority of ordered sphingolipids are typically found in the outer leaflet of the plasma membrane due to the asymmetric localization of cholesterol (Simons and Ehehalt, 2002; Kusumi et al., 2020; Liu et al., 2017), weak signals of inner leaflet lipids were detected between the UPIa and Ib transmembrane domains (Figure S2A). The presence of hexagonally-aligned lipids in the inner leaflet possibly contributes to the AUM's exceptional rigidity. These crystalline lipids in the AUM are likely to play an essential role in the barrier function of the urothelium (see Discussions).

Subunit arrangement of the uroplakin complex

The cryoEM structure of the uroplakin complex reveals that the extracellular domains of both UPII and UPIIIa exhibit distinctive beta-sheet structures (Figure 2A, B, D), which could have functional implications in protein binding or adhesion of pathogens. With these extracellular

116 domains of UPII and UPIIIa, uroplakin heterotetramer overall adopts a Y-shaped conformation,
117 which creates a substantial groove that may also provide a binding interface for other proteins
118 (Figure S2A, white arrow). Adjacent heterotetramers are connected through arches formed by
119 the UPII and UPIIIa extracellular domains. Interestingly, beneath these arches, a channel is
120 present, which is continuous with the central cavity space (Figure S2A, red arrows). The
121 biochemical robustness of the uroplakin hexameric complex, despite its abundance of inner
122 cavities, can likely be attributed to the reinforcement provided by the lipid domains.
123 The prevailing hypothesis concerning the subunit arrangement of the uroplakin complex
124 suggests that Ia/II and Ib/IIIa heterodimers form the inner and outer subdomains, as inferred
125 from electron microscopy studies of FimH-bound AUM (Zhou et al., 2001; Min et al., 2002).
126 However, our high-resolution reconstruction revealed that Ia/II and Ib/IIIa heterodimers
127 constitute the outer and inner subdomains, respectively (Figure 2A). Additionally, it has been
128 reported that the cleavage of UPII at Arg84 by furin results in the removal of the N-terminal
129 pro-sequence (amino acids 25-84) from the uroplakin complex (Lin et al., 1994; Hu et al.,
130 2005). However, our findings suggest that the prosequence forms the external surface of the
131 complex through the formation of several beta sheets (Figure S2B). Moreover, our
132 reconstruction uncovered the presence of carbohydrate chains on six N-glycosylated residues,
133 namely UPIa Asn169, UPIb Asn131, UPII Asn28, Asn57, UPIIIa Asn139, and Asn170 in
134 accordance with previous studies (Figure S3) (Hu et al., 2005; Kanik-Prastowska et al., 2014;
135 Wu et al., 1995). Previous electron microscopy studies have suggested that UPIa Asn169,
136 functioning as the binding site for the bacterial FimH protein, is located at the apex of the inner
137 subdomain (Min et al., 2002; Xie et al., 2006). However, our reconstruction placed this
138 glycosylated residue on the external surface of the uroplakin complex. Our structural analysis
139 of the FimH-bound uroplakin complex also supports this assignment, as it demonstrates a weak
140 additional density in the vicinity of Asn169 of UPIa (Figure 7B, arrowheads). Although a

141 previous cryo-electron microscopy study of tannic-acid-stained uroplakin complexes reported
142 alterations in the transmembrane helices (Wang et al., 2009), our analysis of the FimH-bound
143 uroplakin structure did not detect any discernible conformational changes (Figure 7) (see
144 Discussion).
145
146 *Inter-subunit interactions within the uroplakin complex*
147 Our map and model suggest that the hexameric complex is assembled through three inter-
148 subunit interfaces: the Ia-Ib, II-IIIa, and IIIa-IIIa interfaces. The Ia-Ib interface appears similar
149 to that reported in the PRPH2-ROM1 tetraspanin complex (Figure 4A) (El and Gros, 2022).
150 The interface is stabilized by various interactions, including a hydrophobic interaction between
151 Phe196 of UPIa and Leu155 of UPIb (Figure 4B), and a hydrogen bond between Asn195 of
152 UPIa and Gln130 of UPIb (Figures 4C and 4D). The resolution of the II-IIIa interface,
153 particularly near the flexible loop 90-101 of UPII, is of lower quality. However, it appears to
154 be stabilized by a hydrophobic cluster of a disulfide bond between Cys51-80 and Pro79 of UPII,
155 a disulfide bond between Cys47-Cys110, and Leu113 of UPIIIa (Figure 5A).
156 Finally, the UPIIIa extends its loop 137-161 into the groove of an adjacent IIIa, forming an
157 interface stabilized by a hydrophobic cluster composed of Pro146 of IIIa, Leu66, and Trp182
158 of the adjacent IIIa (Figures 5B). Additionally, a hydrophobic cluster between the
159 transmembrane helices of UPIa and Ib appears to stabilize the heterotetramer (Figure 5C).
160 These multiple interactions are thought to contribute to the highly rigid nature of the uroplakin
161 complex and the AUM.
162
163 *Lipidomic analysis of the AUM*
164 A lipidomic analysis was conducted to discern the lipid species comprising the characteristic
165 paracrystalline array of the AUM. The lipid composition of the sarkosyl-insoluble fraction,

166 primarily consisting of the AUM, was compared to that of the total urothelial membrane
167 homogenates (Figure 6 and Supplemental spread sheet 1). The results, as depicted by the LC-
168 MS profile, revealed the enrichment of hexosylceramides in the AUM, in accordance with the
169 previous studies (Hicks et al., 1974; Stubbs et al., 1979; Watanabe et al., 2022). We also
170 observed enrichment of ceramides, which is likely to be fragmentation products of ionization.
171 These results suggest that the hexagonally-arranged lipid domain is composed of
172 hexosylceramides.
173
174 *Structure of FimH-bound uroplakin complex*
175 We have solved the structure of the uroplakin complex in association with FimH (Figure 7,
176 Wang et al., 2009). Binding of FimH to the AUM was confirmed by SDS-PAGE and
177 fluorescence microscopy (Figure S4A and B). Initially, the FimH-bound map displayed a lower
178 resolution and weaker lipid densities compared to the FimH-unbound map (Figure S4C, pre-
179 3D classification). To enhance resolution and clarify the lipid array, we employed 3D
180 classification, resulting in a higher resolution map (Fig. 7A and S4C, class #1). However, no
181 significant structural differences were discernible between the FimH-bound and unbound maps
182 (Figure 7A and B). In the lower resolution class #2 and #3 maps, lacking the hexagonal
183 crystalline lipid array, we identified additional densities adjacent to UPIa Asn169 (Figure 7B,
184 arrowheads). These are hypothesized to represent bound FimH components and/or FimH-
185 stabilized carbohydrate chains. Our findings suggest that FimH binding may modify the
186 uroplakin-lipid array arrangement without affecting the uroplakin complex conformation.
187
188 **Discussion**
189 The structures of the AUM and the uroplakin have been extensively analyzed utilizing electron
190 microscopy (Min et al., 2006; Min et al., 2003; Min et al., 2002; Walz et al., 1995; Zhou et al.,

191 2001). One of the studies achieved a resolution of approximately 6 Å in the membrane plane,
192 yet the vertical resolution was limited to 12.5 Å, thus failing to uncover the residue-level
193 information (Min et al., 2006). This limited structural information led to incorrect subunit
194 assignment of the uroplakin (Min et al., 2002). The Ia/II heterodimer has long been believed to
195 form the inner subdomain of the uroplakin hexameric complex based on the observation of
196 additional densities in the difference map between the uroplakin structures with and without
197 bound FimH, which interacts with glycosylated UPIa (Zhou et al., 2001). However, our
198 reconstruction revealed that these "additional densities" are likely artifacts of the low-
199 resolution EM maps, as the Ia/II heterodimer actually constitutes the outer subdomain of the
200 uroplakin (Figure 2A and S2B).
201
202 Reports indicate that the binding of FimH to UPIa instigates conformational alterations within
203 the transmembrane domains of uroplakin (Wang et al., 2009). Contrarily, our analysis of the
204 FimH-bound uroplakin structure did not reveal any significant conformational modifications
205 (Figure 7). The inherent flexibility of the carbohydrate chain coupled with the rapid on/off
206 kinetics of FimH-mannose binding pose substantial challenges in visualizing the attached
207 FimH and any resultant conformational changes (Lee et al., 2015; Prestegard, 2021; Sauer et
208 al., 2016). The observed degradation in resolution within FimH-bound maps hints at potential
209 alterations in the configuration of the uroplakin complex and/or lipid crystalline array.
210 Variations in the fluidity or organization of the crystalline lipid membrane have been known
211 to trigger signal transduction (Desai and Miller, 2018; Los and Murata, 2004). Given the
212 apparent accommodation of FimH molecules within the interstitial space between two adjacent
213 uroplakin complexes (Figure S4D), the ensuing molecular packing or crowding of FimH-bound
214 uroplakin complexes could exert tension on the AUM, thereby eliciting cellular responses
215 (Balogh et al., 2005; Zhang et al., 2021). However, the precise mechanism through which the

216 attachment of FimH to the flexible carbohydrate chain induces intracellular signaling remains
217 an open question for further exploration (Thumbikat et al., 2009).
218
219 Intriguingly, the prosequence of UPII persists within the mature uroplakin complex (Figure
220 S2C). The precursor form of UPII, which has a molecular weight of 29 kDa, is cleaved by the
221 enzyme furin in the trans-Golgi network. This results in the separation of the N-terminal
222 glycosylated prosequence and the "mature" UPII, which lacks glycosylation and has a
223 molecular weight of 15 kDa (Lin et al., 1994; Hu et al., 2005; Kanik-Prastowska et al., 2014).
224 However, it has been documented that the S2' fragment of SARS-CoV-2 spike protein remains
225 associated with the molecule after cleavage by furin (Ord et al., 2020; Johnson et al., 2021).
226 This observation holds true for the UPII prosequence. The question arises as to why only a
227 single UPII band was observed in the electrophoresis of the AUM. One potential explanation
228 is that the estimated molecular weight of the glycosylated UPII prosequence is roughly 14 kDa,
229 and thus it may align with the 15 kDa band. Another possibility is that the heterogeneous nature
230 of the glycosylation chains, which make up over half of the prosequence's mass, may not
231 produce a distinguishable band in the electrophoresis.
232
233 The epithelial lining of the bladder demonstrates a distinct impermeability to water, protons,
234 and urea, effectively preventing the infiltration of urinary substances into the surrounding tissue
235 (Negrete et al., 1996; Lavelle et al., 1998). Depletion of uroplakin complexes from the
236 urothelial apical membrane by UPIII knockout leads to a two-fold increase in water
237 permeability. Yet, the urothelial barrier maintains a substantial degree of resistance to water
238 and urea permeation (Hu et al., 2002). These observations imply that the lipids and the
239 uroplakin exert complementary influences on the barrier properties of the urothelial apical
240 membrane. Our lipidomic analysis revealed an enrichment of hexosylceramide in the AUM

241 (Figure 6) (Stubbs et al., 1979). Previous studies have established that ceramides tend to
242 associate with each other, and an accumulation of these molecules can form a liquid crystalline
243 phase (Huang et al., 1996; Ghysels et al., 2019). The formation of ceramide-enriched
244 crystalline lipid domains has also been linked to the clustering of CD95 (Grassme et al., 2001;
245 Grassme et al., 2001). These findings suggest that the accumulation of hexosylceramides in the
246 AUM may play a role in the formation of a hexagonal lattice structure of uroplakin (Min et al.,
247 2003).
248 Molecular dynamics simulations have predicted that sphingolipids form hexagonally arranged
249 liquid-ordered phases (Sodt et al., 2015; Ghysels et al., 2019). The yeast plasma membrane
250 H+-ATPase, Pma1 hexamer, has been demonstrated to encircle a liquid-crystalline membrane
251 microdomain (Zhao et al., 2021). Our findings represent the first direct visualization of
252 hexagonally organized liquid crystalline membrane domains in mammalian cells. Although the
253 liquid-ordered phase of the lipid domain is believed to be essentially impermeable to water and
254 ions, small molecules can traverse the membrane at the boundary between ordered and
255 disordered domains (Ghysels et al., 2019; Gensure et al., 2006). It is noteworthy that the
256 uroplakin-free hinge regions that connect the neighboring AUM plaques also exhibit resistance
257 to sarkosyl and alkali treatments, indicating highly specialized structures (Liang et al., 1999).
258 These hinge regions may serve to prevent the penetration of small molecules at the boundary
259 between the plaques.
260
261 While our team was successful in constructing a model of the uroplakin complex, we
262 encountered a limitation in the resolution of the vertical dimension, which hindered our ability
263 to confidently determine the precise positioning of the side chains. To overcome this challenge,
264 we propose the utilization of high-resolution subtomogram averaging, as it has the capability
265 to bypass the overlap of molecules in the high-tilt views. However, to effectively implement

266 this technique, it is imperative to devise an advanced algorithm that can accurately rectify the
267 significant deformation of the AUM caused by irradiation.
268
269 **Methods**
270 *Isolation of porcine AUM*
271 Fresh porcine bladders were obtained from a local slaughterhouse. The AUM was isolated
272 according to the previous study with modifications (Liang et al., 1999). The urothelium was
273 scraped from the luminal surface with a medicine scoop and suspended in ice-cold PBS. After
274 centrifugation at 1,500 ×g at 4 ℃ for 5 minutes, the pellets were homogenized with a Dounce
275 glass homogenizer in buffer A (10 mM Hepes, pH 7.4, 1 mM EDTA, and protease inhibitor
276 cocktail). After centrifugation at 2,500 × g at 4 ℃ for 10 minutes, the pellets were resuspended
277 in buffer A, loaded onto a 1.6 M sucrose cushion, and centrifuged at 46,000 ×g at 4 ℃ for 30
278 minutes. The membrane fraction concentrated at the interface was collected, loaded onto a 1.6
279 M sucrose cushion, and centrifuged once again. The collected membrane fraction was
280 resuspended in buffer A plus 2% sarkosyl and incubated at room temperature for 10 minutes.
281 Sarkosyl-insoluble membranes were collected after centrifugation at 18,000 ×g at 4 °C for 30
282 minutes. The pellets were further washed by resuspension in 25 mM NaOH, and centrifuged at
283 18,000 ×g at 4 ℃ for 10 minutes. The pellets of the AUM were washed twice with buffer A
284 and proceeded to electron microscopy.
285
286 *Purification of FimH-FimC complex*
287 The cDNA of *fimH* and its chaperone *fimC* genes were cloned from *E. coli* DH5a into
288 pACYCDuet-1 bicistronic plasmid (Sigma-Aldrich, Burlington, MA), and the resulting co-
289 expression plasmid was introduced to *E coli.* BL21 (DE3) (Pellecchia et al., 1999). The bacteria
290 were grown at 37℃ in LB medium containing chloramphenicol (34 μg/ml). At an OD600 of

291 0.7, IPTG was added to a final concentration of 0.5 mM. The cells were further grown for 18
292 hours at 15℃, harvested by centrifugation, washed by PBS, and disrupted by sonication. After
293 removing cell debris by centrifugation, the supernatant was applied to Ni-NTA resin (Qiagen,
294 Germantown, MD) and eluted with 20 mM Tris-HCl pH 8.0, 0.3 M imidazole. Fractions
295 containing FimH-FimC were pooled and loaded onto a gel filtration column (ProteinArk,
296 Rotherham, UK) equilibrated with 20 mM Hepes-NaOH pH 7.4, 150 mM NaCl. Fractions
297 containing FimH-FimC were dialyzed against buffer A and were concentrated using Vivaspin
298 2 (Sartorius, Göttingen, Germany). For cryo-EM, two times molar-excess FimH-FimC was
299 mixed with the AUM (0.05 mg/ml) and incubated for 1 hour at 4℃ before plunge-freezing.
300
301 *Cryo-electron microscopy of the AUM*
302 The AUM was suspended in buffer A at a concentration of 0.05 mg/ml. 3 µl of the sample was
303 applied to freshly glow-discharged holey carbon grids, Quantifoil R1.2/1.3 Cu/Rh 200 mesh
304 (Quantifoil Micro Tools GmbH, Großlöbichau, Germany), blotted from both sides for 3
305 seconds at 4 ℃ under 99% humidity and plunge frozen in liquid ethane using Vitrobot Mark
306 IV (Thermo Fisher Scientific, Waltham, MA). Images were recorded using a Titan Krios G4
307 microscope at the University of Tokyo (Thermo Fisher Scientific) at 300 keV, a Gatan
308 Quantum-LS Energy Filter (Gatan, Pleasanton, CA) with a slit width of 20 eV, and a Gatan K3
309 BioQuantum direct electron detector in the electron counting mode. The nominal magnification
310 was set to 64,000 × with a physical pixel size of 1.35 Å/pixel. Movies were acquired using the
311 SerialEM software (Mastronarde, 2005), and the target defocus was set to 2.5-4.5 µm for
312 tomography and 1-3 µm for single particle analysis (SPA). For tomography, each movie was
313 recorded for 0.18 seconds with a total dose of 1.26 electrons/ $Å^2$ and subdivided into 10 frames.
314 The angular range of the tilt series was from –60° to 60° with 3.0° increments using the dose-
315 symmetric scheme (Hagen et al., 2017) or the continuous scheme. The total dose for one tilt

316 series acquisition is thus 50 electrons $Å^2$. For SPA, each movie was recorded for 6.7 seconds
317 with a total dose of 50 electrons/ $Å^2$ and subdivided into 50 frames. Specimens were tilted at
318 0, 30, 45, and 55°. The ratio of tilted images was 1:1:2:2 for 0, 30, 45, and 55°, respectively.
319
320 *Fluorescence microscopy of FimH-bound AUM*
321 The AUM suspension (1 mg/ml) was incubated with 0.1 mg/ml FITC-isothiocyanate (Dojindo
322 Laboratories, Kumamoto, Japan) at room temperature for an hour, followed by four buffer A
323 washes via centrifugation to obtain FITC-labeled AUM. Concurrently, FimH-FimC and BSA
324 (2 mg/ml) were incubated with 0.2 mg/ml ATTO 590-NHS-ester (ATTO-TEC GmbH, Siegen,
325 Germany) for an hour at room temperature. Unbound dye was removed using a PD-10 desalting
326 column (cytiva, Marlborough, MA), and the proteins were concentrated using Vivaspin 2. The
327 labeled AUM was then combined with FimH-FimC/BSA and incubated as described above.
328 Quantifoil R1.2/1.3 Cu/Rh 200 mesh grids were prepared by glow-discharging and blocking
329 with 1 mg/ml BSA in buffer A for 3 minutes. A 3µl sample was applied to each grid and plunge-
330 frozen as described above. Post-freezing, the grids were retrieved from the liquid ethane,
331 thawed, and washed four times with buffer A. Finally, the grids were immersed in mounting
332 buffer (buffer A supplemented with 50% glycerol and 0.1M dithiothreitol) and visualized using
333 a BX53 fluorescence microscope (Olympus/Evident, Tokyo, Japan).
334
335 *Data processing for tomography*
336 Movies were subjected to beam-induced motion correction, image alignment, CTF correction,
337 and reconstruction by back-projection using the IMOD software package (Kremer et al., 1996).
338 Tomograms were 8 × binned and the centers of each uroplakin particle were manually selected
339 using 3dmod tool. Volumes with 30-pixel^3 dimensions were extracted from 8 × binned
340 tomograms and were averaged using the PEET software (Nicastro et al., 2006). A randomly

341 selected subtomogram was used for the initial reference. Alignments were repeated twice for
342 8×binned and once for 4×binned tomograms with 60-pixel^3 dimensions. The averaged
343 subtomogram was used for the reference in the subsequent SPA.
344
345 *Data processing for SPA*
346 Image analysis was executed utilizing CryoSPARC v4.2.1 (Punjani et al., 2017), as depicted
347 in Figure S1A. Images, 4× binned at 128 pixels^2, were selected and extracted from motion-
348 corrected and CTF-corrected micrographs, leveraging the projections of the mean
349 subtomogram as templates. The particle stack underwent rigorous purification through five
350 iterations of 2D classification and three cycles of heterogeneous refinement. Post local motion
351 correction and CTF refinement, a homogenous refinement of the unbinned 512 pixels^2 particles
352 produced a global resolution of 5 Å. Notably, at this juncture, the crystalline lipids remained
353 undetected. To enhance the resolution, six uroplakin particles encircling the central particle
354 were removed. The ensuing local refinement achieved a global resolution of 3.5 Å, revealing
355 the crystalline lipids. The AUM's peripheries frequently exhibited folding, influencing the
356 orientation distribution. Yet, the superimposed molecules affected the accuracy of the lateral
357 view alignment. Resolutions in both transverse and vertical directions were ascertained using
358 CryoSPARC's 3DFSC function (refer to Fig. S1B). The Root Mean Square Deviation (RMSD)
359 between dual models was determined via UCSF Chimera X. Regarding the FimH-bound
360 structure, our analysis mirrored the methodology applied to the unbound structure, extending
361 to particle subtraction and local refinement (see Figure S4C). To augment resolution, we
362 adopted a reference-free and alignment-free 3D classification using CryoSPARC. Class #1
363 displayed the hexagonal crystalline lipid array, whereas Class #2 and #3 presented lipids
364 proximate to the uroplakin complex. Class #3 distinctly exhibited additional densities adjacent
365 to UPIa's Asn169. Efforts to amplify the resolution of these supplementary densities through

366 targeted 3D classification did not result in any signal intensity enhancement.

367

368 *Model building*

369 The initial model was generated using AlphaFold-multimer (Jumper et al., 2021; Mirdita et al.,
370 2022; Evans et al., 2022) and the *Sus scrofa* UPIa, UPIb, UPII, and UPIIIa sequences (Kwon
371 et al., 2011; Visnjar et al., 2017). The AlphaFold-predicted model was refined using PHENIX
372 (v.1.19.2-4158) real-space refinement tool with the secondary structure restraints and
373 Ramachandran restraints on (Liebschner et al., 2019; Afonine et al., 2018). Carbohydrates were
374 added to the Asn residues at the N-Glycosylation sites using Coot (v. 9.8.7) (Emsley et al.,
375 2010; Emsley and Crispin, 2018). The models were further refined using UCSF Chimera,
376 ChimeraX, and ISOLDE (Pettersen et al., 2004; Pettersen et al., 2021; Goddard et al., 2018;
377 Croll, 2018). The refined model was validated using the comprehensive validation tool on
378 PHENIX. Models of ceramide (CCD ID: 16C) and sphingosine (CCD ID: SPH) were fitted
379 manually and refined using ISOLDE.

380

381 *Lipidomic analysis*

382 The lipid composition of the isolated AUM was analyzed using LC-MS. The total urothelium
383 membrane homogenate was used as a control. Lipids were extracted by adding 2-propanol
384 (50:1 by volume to control homogenate or 500 μL to AUM preparation). After centrifugation
385 (10,000 ×g, 10 min, 4C), the supernatant was further diluted (1:10) by 2-propanol, and 3 μL
386 was analyzed by LC-MS. The LC-MS system consisted of an Acquity UPLC system (Waters,
387 Milford, MA), connected to an Exactive mass spectrometer equipped with a HESI-II ion source
388 (Thermo Scientific, Waltham, MA). An Acquity UPLC BEH C8 column (1.0×100 mm,
389 Waters) was used for reversed-phase chromatography with binary gradient elution with mobile
390 phase A (10 mM ammonium formate in acetonitrile/water/formic acid (60/40/0.1)) and B (10

391 mM ammonium formate in 2-propanol/acetonitrile/water/formic acid (90/9.5/0.5/0.1)) at a
392 flowrate of 100 μL/min. Following time program was used [time (%B)]: 0 min (30%) – 12 min
393 (55%) – 18 min (70%) – 20 min (80%) – 22 min (99%) – 27 min (99%) – 27.1 min (30%) –
394 28.5 min (30%). MS was operated in following conditions to perform data-independent, all-
395 ions fragmentation (AIF) MS/MS acquisition: ionization polarity, positive and negative; scan
396 range, 100-2,000 m/z; mass resolution, 25,000; maximum injection time, 500 ms; AGC target,
397 balanced (1×10^6); in-source CID voltage, 0 V (off) and 35 V. MS-DIAL 4.9 software (Tsugawa
398 et al., 2020). was used for peak detection, MS/MS deconvolution, alignment, integration, and
399 lipid identification, of multiple samples. Lipid identification was based on searching lipid
400 database provided with the software, with accurate mass tolerance of 0.005Da and 0.01Da for
401 MS and MS/MS, respectively. For multiple candidates, those with highest score were adopted.
402 No manual curation was performed for individual identifications, as the results were only used
403 to estimate lipid classes abundant in AUM preparation. Peak intensities were normalized using
404 built-in function of MS-DIAL, based on total signal for identified lipids (mTIC). R version 4.2
405 software was used for differential analysis using normalized peak intensity data exported from
406 MS-DIAL. Fold enrichment values were calculated as a ratio for AUM versus control using
407 triplicate, independently prepared samples.
408
409 **Data availability**
410 The map and the model are available on the EMDB under the following accession numbers:
411 EMD-36340 , and PDB 8JJ5.
412 **Ethics & Inclusions statement**
413 This research strictly followed the ethical guidelines and standards established by our
414 institutions, University of Yamanashi and the University of Tokyo, located in Japan. The entire
415 research process, from study design and implementation to data ownership and the authorship

of publications, was carried out exclusively by the authors listed, all of whom are researchers at the aforementioned institutions. As this research was conducted in Japan, by Japanese researchers, it is both locally relevant and compliant with local standards and regulations. The roles and responsibilities of each researcher were established and agreed upon at the outset of the research process. We did not undertake capacity-building plans for external researchers, as our team had all the necessary capabilities to conduct this research. The research has not been restricted or prohibited within our local context. Therefore, there was no need for any special exceptions or permissions to be sought from local stakeholders. Our research does not involve any elements that could lead to stigmatization, incrimination, discrimination, or personal risk to participants. It also does not pose any health, safety, security, or other risk to the researchers involved. The research did not involve the transfer of any biological materials, cultural artefacts, or associated traditional knowledge out of Japan. Hence, no benefit sharing measures were discussed or required. In the formulation of our research and the analysis of our results, we have considered and cited local and regional research relevant to our study.

Acknowledgements

We thank Mrs. Natsuko Maruyama (University of Yamanashi) for technical assistance. This research is partially supported by Platform Project for Supporting Drug Discovery and Life Science Research (Basis for Supporting Innovative Drug Discovery and Life Science Research (BINDS)) from Japan Agency for Medical Research and Development (AMED) under Grant Numbers JP22ama121002 and JP23ama121002 (support number 2639). This work was supported by the Takeda Science Foundation (to T.O.), the Daiichi Sankyo Foundation of Life Science (to T.O.), the Japan Society for the Promotion of Science (KAKENHI Grant numbers JP21H02654, JP22H05538 (T.O.), JP21H05248 (M.K.)), and the Naito Foundation (to T.O.). Molecular graphics and analyses performed with UCSF ChimeraX, developed by the Resource

for Biocomputing, Visualization, and Informatics at the University of California, San Francisco, with support from National Institutes of Health R01-GM129325 and the Office of Cyber Infrastructure and Computational Biology, National Institute of Allergy and Infectious Diseases.

447 **Figures and Legends**

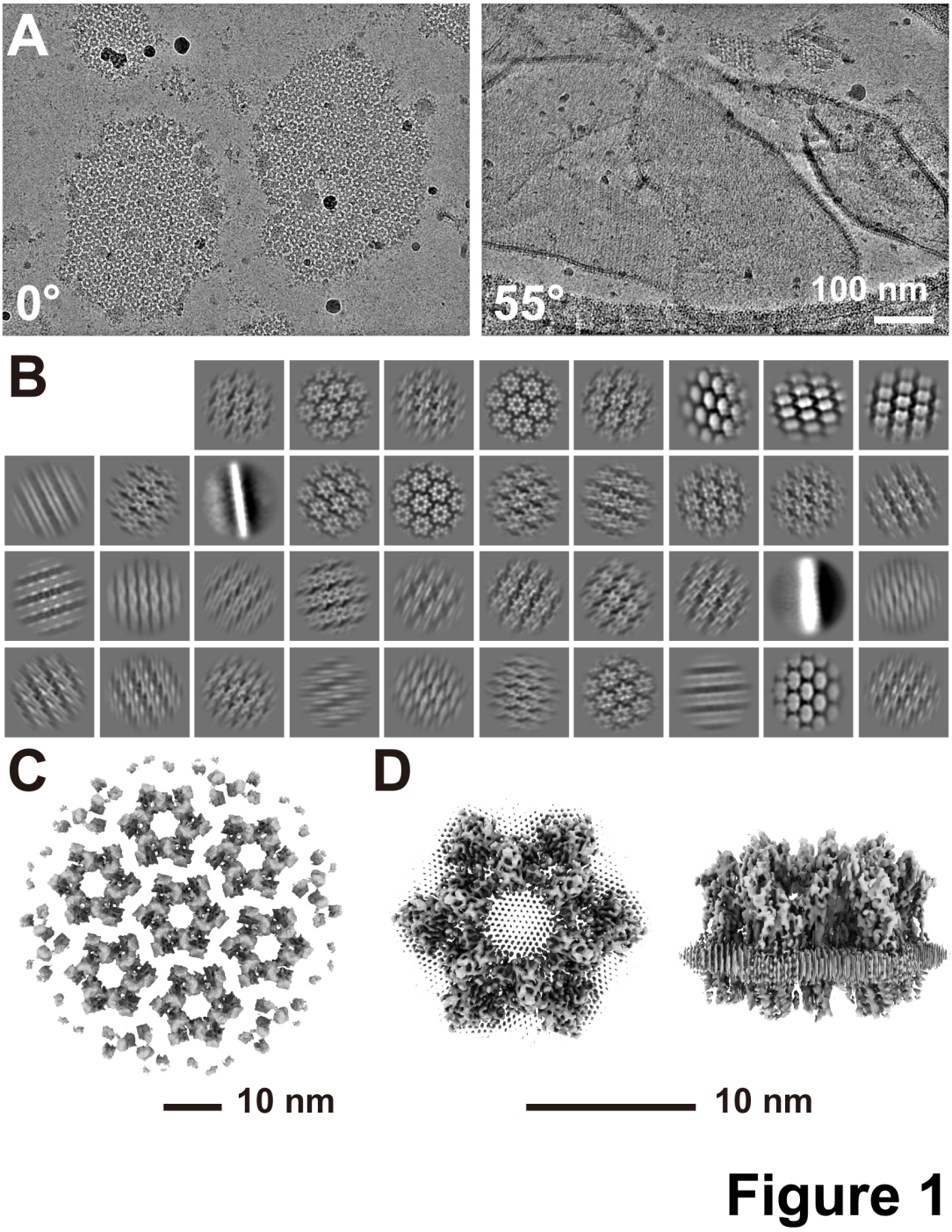

448

449 **Figure 1: Cryo-electron microscopy of the AUM.** (A) Representative micrographs of the
450 AUM. Tilt angles are indicated. (B) 2D class averages of the particles. (C) Reconstructed
451 hexagonal array of the uroplakin complex. (D) Local refinement of the central uroplakin
452 complex. Top and side views are shown. Hexagonally-aligned crystalline lipids are visualized.

453

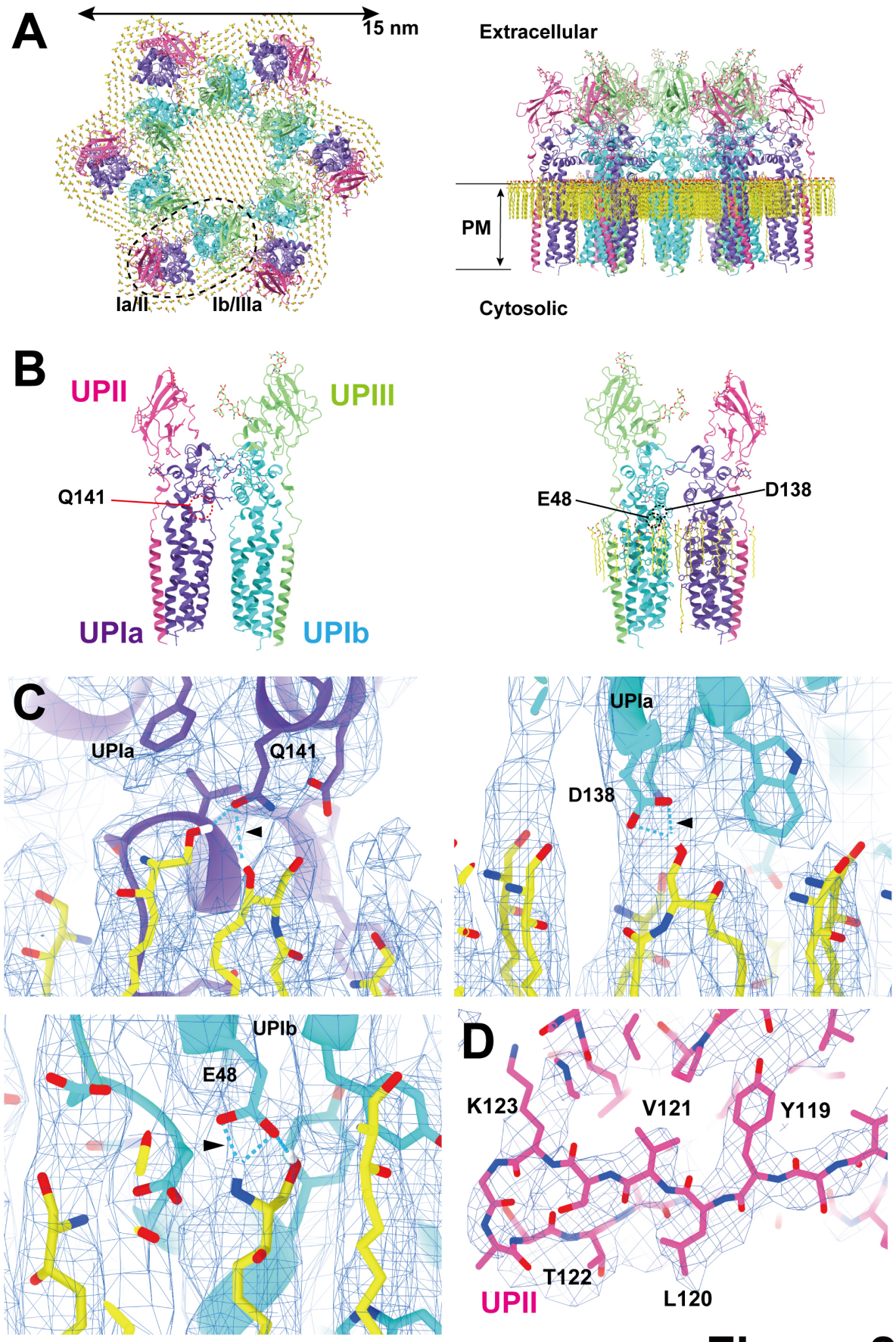
A
15 nm
Ia/II
Ib/IIIa
Extracellular
PM
Cytosolic
B
UPII
UPIII
Q141
UPIa
UPIb
E48
D138
C
UPIa
Q141
UPIa
D138
UPIb
E48
D
K123
V121
Y119
T122
UPII
L120

Figure 2

454

Figure 2: Models of the uroplakin complex and the crystalline lipids. (A, B) Models of the hexameric complex (A) and single heterotetramer (B) are shown. An initial model was predicted using AlphaFold and real-space refined using PHENIX and ISOLDE. Lipid models (C16 ceramide or sphingosine) were manually fitted and refined using ISOLDE. Note that the models of sphingolipids and ceramides are placed tentatively. The precise identities of these lipids within the structure remain uncertain. Purple: UPIa; cyan: UPIb; pink: UPII; green: UPIIIa; and yellow: lipids. (B) Residues magnified in C are indicated. (C) Possible interactions between the side chains and the lipid head groups were indicated. (D) Beta-sheet of UPII with discernible side-chains.

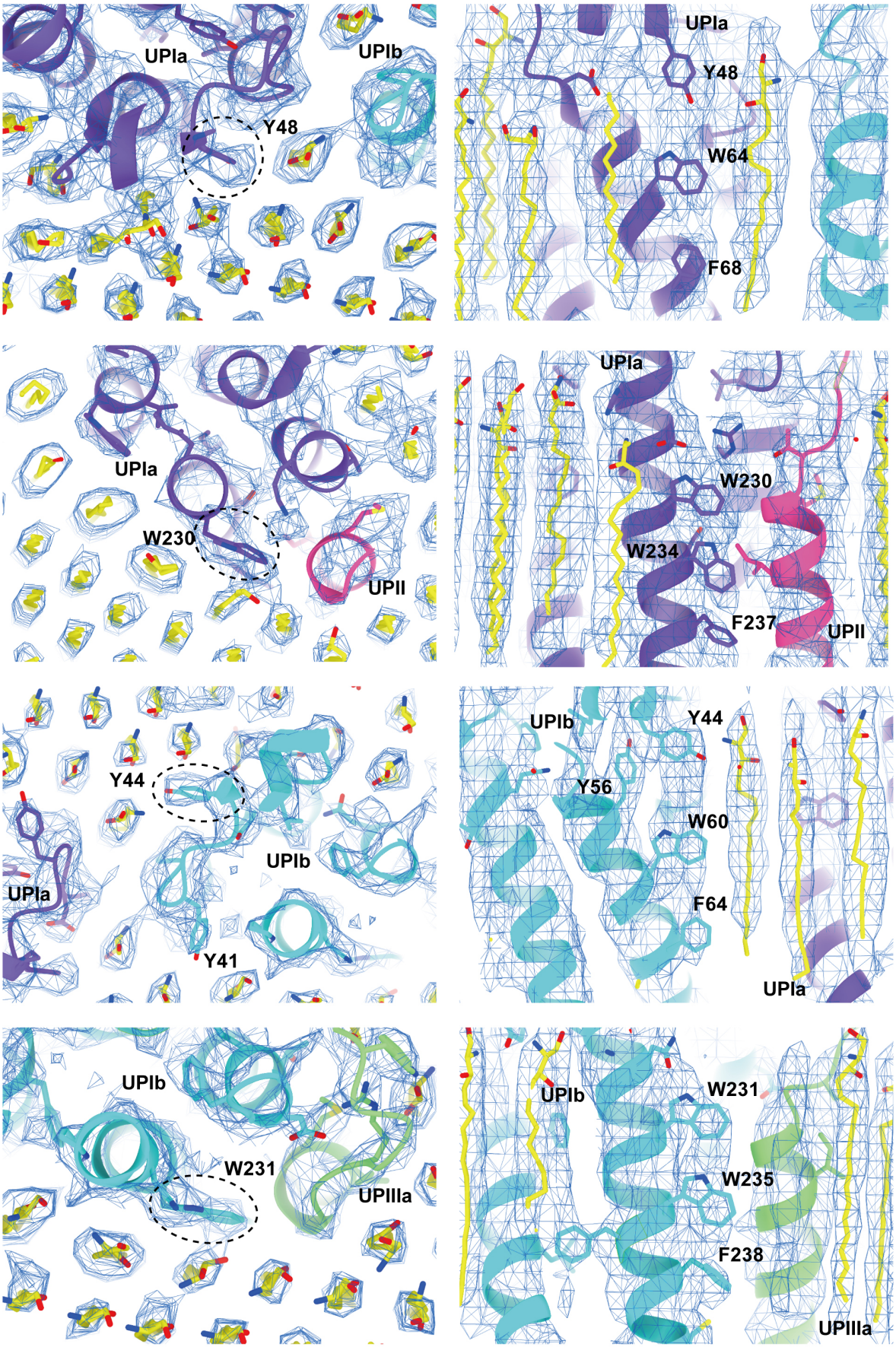
UPIa
UPIb
Y48
UPIa
Y48
W64
F68
UPIa
W230
UPII
UPIa
W230
W234
F237
UPII
Y44
UPIb
UPIa
Y41
UPIb
Y44
Y56
W60
F64
UPIa
UPIb
W231
UPIIIa
UPIb
W231
W235
F238
UPIIIa

Figure 3

464

465 **Figure 3: Interactions between the UPIa/Ib transmembrane helices and the lipids.**
466 Vertically-aligned bulky side chains appear to be incorporated into the crystalline lipids. Top
467 (left) and side (right) views are shown.

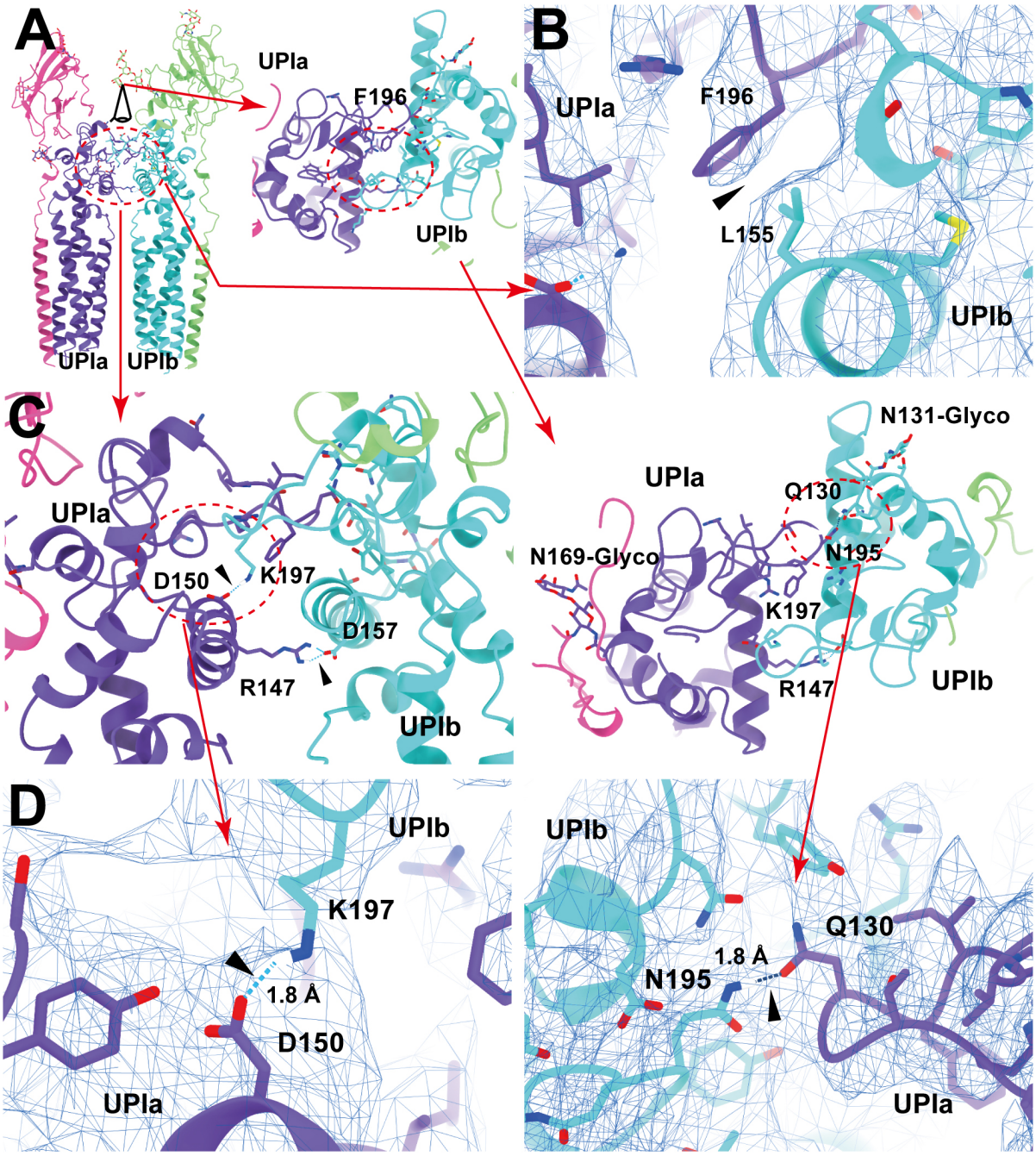

468

469 **Figure 4: UPIa-Ib interface.** (A) The interface between UPIa and Ib is characterized by two
470 opposing helices (broken circles). Top views (A, C, and D, right) are shown. (B) Hydrophobic

interaction between UPIa F196 and Ib L155 (arrowhead). (C and D) Hydrogen bonds between UPIa D150 - Ib K197, Ia R147 - Ib D157, and Ia N195 - Ib Q130 are indicated (arrowheads). The bond between Ia R147 - Ib D157 is less reliable due to its weak densities. (D) The electron densities of the hydrogen bonds are shown in mesh. Distances are indicated.

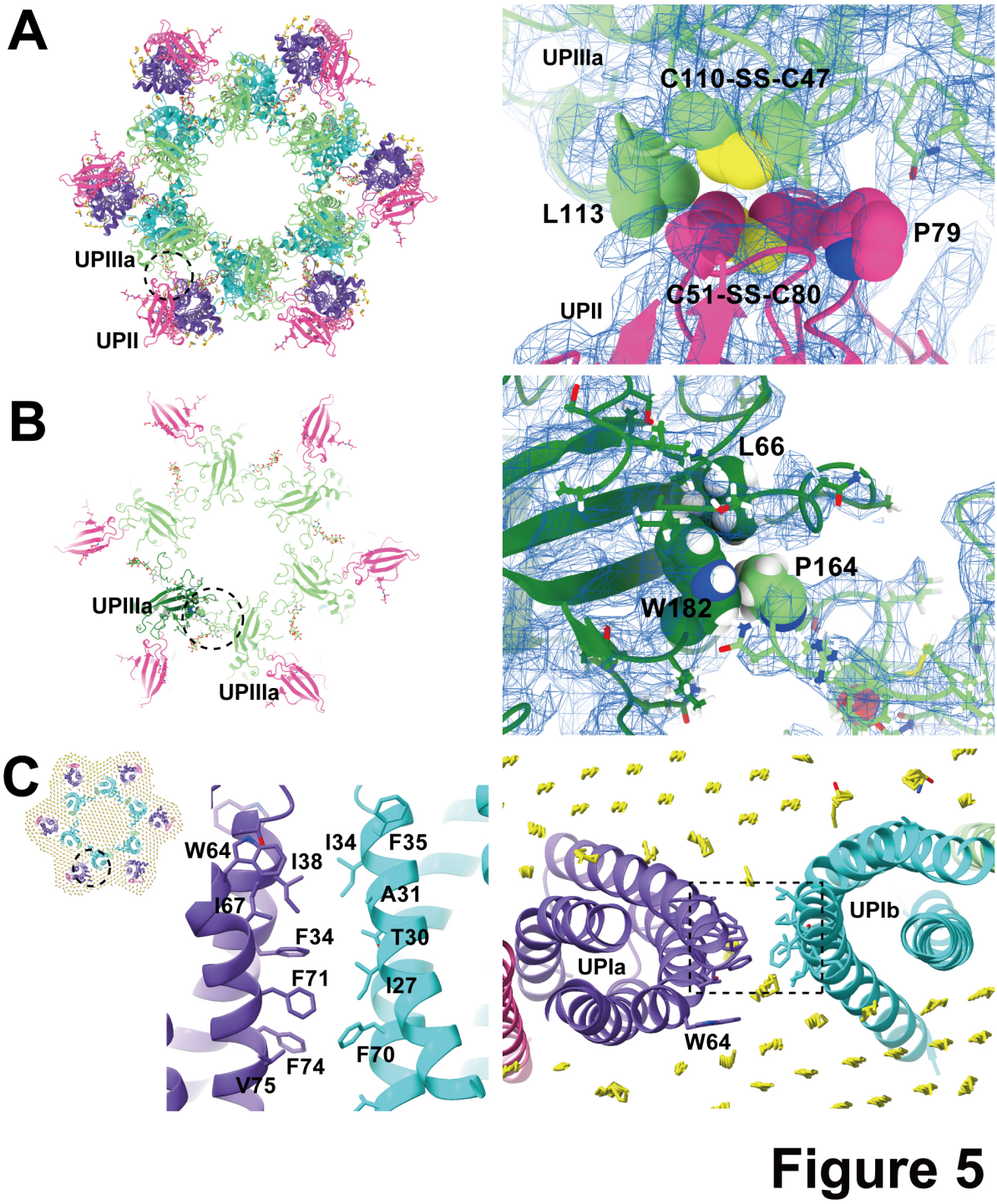

Figure 5: **UPII-IIIa, IIIa-IIIa, and the intra-membrane interfaces.** (A) Hydrophobic

interaction between UPII and IIIa. Disulfide bonds between Cys51-Cys80 of UPII and between Cys47-Cys110 of IIIa are facing each other, and the interface appears to be supported by Pro79 of UPII and Leu113 of IIIa. (B) IIIa-IIIa interface. Pro164 at the apex of the loop 137-161 of IIIa (arrows) inserts into the groove of Leu66 and Trp182 of the adjacent IIIa. (C) The interface between the transmembrane helices of Ia and Ib. At the pseudo-symmetric center of Ia and Ib (broken circle, right), a cluster of hydrophobic side chains mediates the Ia-Ib interaction.

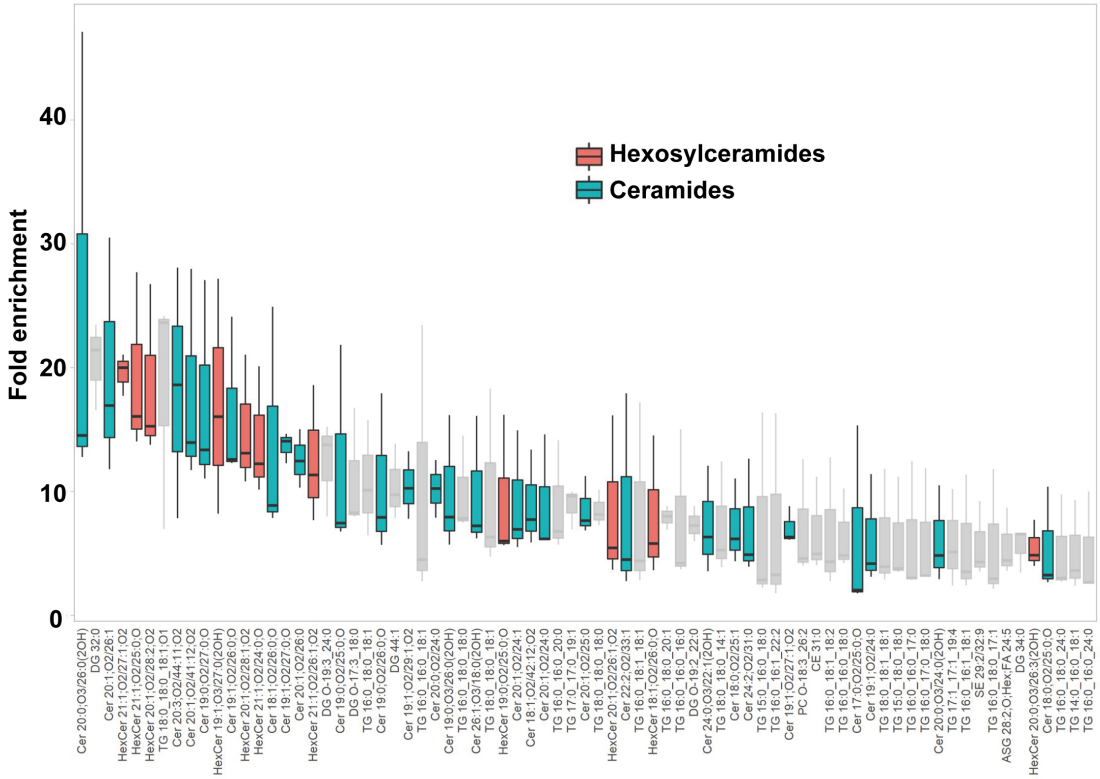

Figure 6

Figure 6: **Lipidomic analysis of the AUM.** The chart displays the fold-enrichment of each lipid species detected in the sarkosyl-insoluble AUM fraction relative to the whole bladder scrape. Lipids were extracted from both sample types and analyzed using liquid chromatography-mass spectrometry (LC-MS). The peak heights were normalized by dividing them by the total signal for all identified lipids for each experiment. The fold-enrichment values indicate the difference in relative abundance of each lipid species in the sarkosyl-insoluble AUM fraction compared to the whole bladder scrape, with higher values suggesting an

491 enrichment in the AUM fraction. The result for positive ion mode is shown. Data represent the

492 mean fold-enrichment and standard deviation from three independent experiments (n = 3).

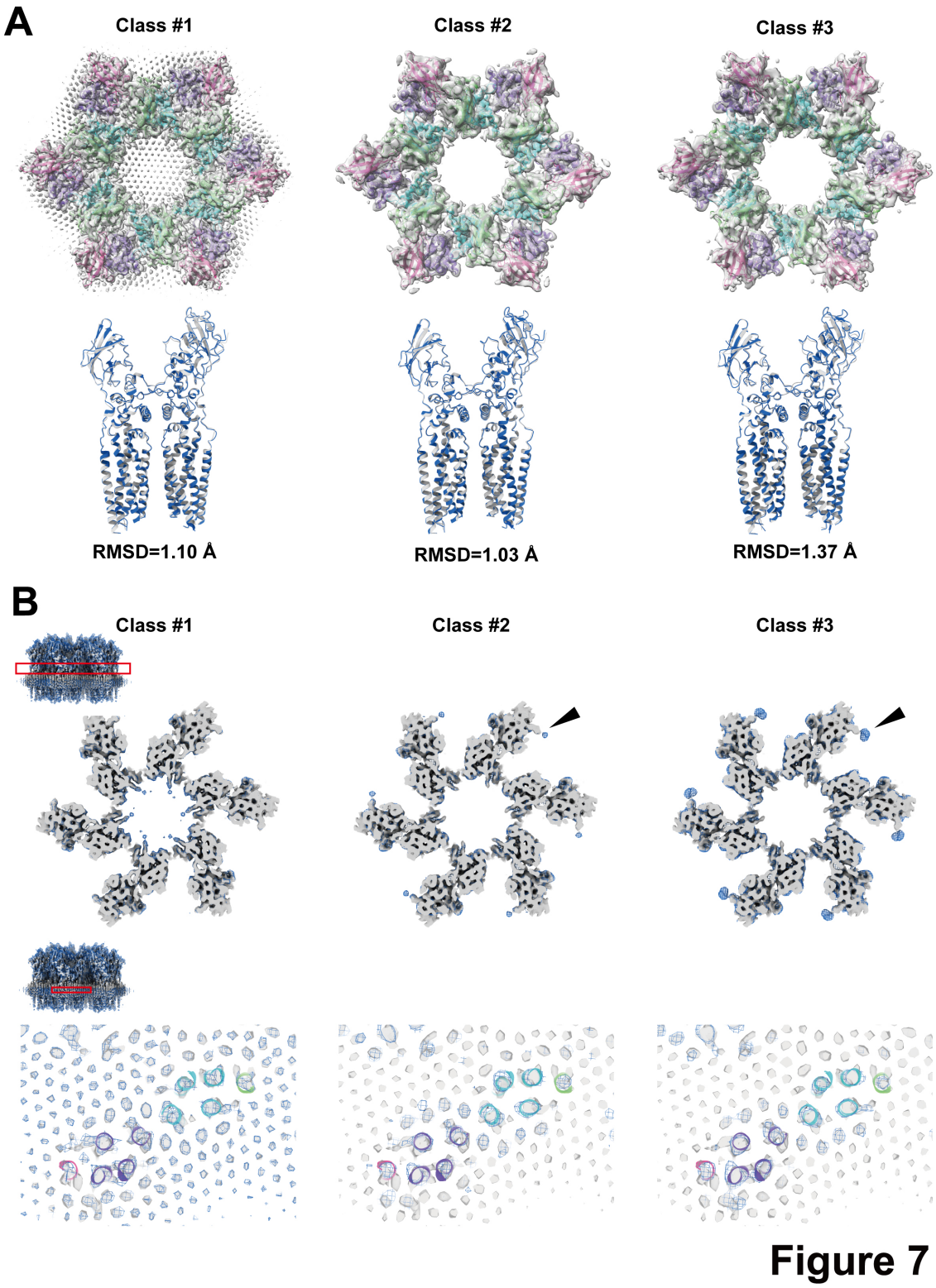

493

494 **Figure 7**: **FimH-bound structure of the uroplakin complex.** (A) Map and fitted models of

495 FimH-bound structure (class #1). (C) Comparison between models of FimH-bound (blue) and

unbound (gray). RMSD between the two models was 0.962 Å. (D) Slab sections of FimH-bound maps (classes #1-3) superimposed to FimH-unbound map. Blue mesh: FimH-bound; gray surface: FimH-unbound. Red rectangles of the upper-left inset indicate the positions of the slabs. (D, top) Slabs at the height of UPIa N169 show extra densities (arrowheads). (D, bottom) Slabs at the height of the transmembrane helices show no structural differences.

503 **References**

504 Hicks, R.M. 1965. The fine structure of the transitional epithelium of rat ureter. *J. Cell. Biol.*
505 **26**, 25-48.

506 Hicks, R.M., Ketterer, B., and Warren, R.C. 1974. The ultrastructure and chemistry of the
507 luminal plasma membrane of the mammalian urinary bladder: a structure with low
508 permeability to water and ions. *Philos. Trans. R. Soc. Lond. B. Biol. Sci.* **268**, 23-38.

509 Frank, J., Goldfarb, W., Eisenberg, D., and Baker, T.S. 1978. Reconstruction of glutamine
510 synthetase using computer averaging. *Ultramicroscopy.* **3**, 283-290.

511 Stubbs, C.D., Ketterer, B., and Hicks, R.M. 1979. The isolation and analysis of the luminal
512 plasma membrane of calf urinary bladder epithelium. *Biochim. Biophys. Acta.* **558**, 58-72.

513 Radermacher, M. 1988. Three-dimensional reconstruction of single particles from random
514 and nonrandom tilt series. *J. Electron. Microsc. Tech.* **9**, 359-394.

515 Hultgren, S.J., Abraham, S., Caparon, M., Falk, P., St, Geme JW 3rd, and Normark, S. 1993.
516 Pilus and nonpilus bacterial adhesins: assembly and function in cell recognition. *Cell.* **73**,
517 887-901.

518 Lin, J.H., Wu, X.R., Kreibich, G., and Sun, T.T. 1994. Precursor sequence, processing, and
519 urothelium-specific expression of a major 15-kDa protein subunit of asymmetric unit
520 membrane. *J. Biol. Chem.* **269**, 1775-1784.

521 Yu, J., Lin, J.H., Wu, X.R., and Sun, T.T. 1994. Uroplakins Ia and Ib, two major
522 differentiation products of bladder epithelium, belong to a family of four transmembrane
523 domain (4TM) proteins. *J. Cell. Biol.* **125**, 171-182.

524 Walz, T., Häner, M., Wu, X.R., Henn, C., Engel, A., Sun, T.T., and Aebi, U. 1995. Towards
525 the molecular architecture of the asymmetric unit membrane of the mammalian urinary
526 bladder epithelium: a closed "twisted ribbon" structure. *J. Mol. Biol.* **248**, 887-900.

527 Wu, X.R., Medina, J.J., and Sun, T.T. 1995. Selective interactions of UPIa and UPIb, two

528 members of the transmembrane 4 superfamily, with distinct single transmembrane-domained
529 proteins in differentiated urothelial cells. *J. Biol. Chem.* **270**, 29752-29759.
530 Huang, H.W., Goldberg, E.M., and Zidovetzki, R. 1996. Ceramide induces structural defects
531 into phosphatidylcholine bilayers and activates phospholipase A2. *Biochem. Biophys. Res.*
532 *Commun.* **220**, 834-838.
533 Kremer, J.R., Mastronarde, D.N., and McIntosh, J.R. 1996. Computer visualization of three-
534 dimensional image data using IMOD. *J. Struct. Biol.* **116**, 71-76.
535 Negrete, H.O., Lavelle, J.P., Berg, J., Lewis, S.A., and Zeidel, M.L. 1996. Permeability
536 properties of the intact mammalian bladder epithelium. *Am. J. Physiol.* **271**, F886-894.
537 Hooton, T.M., and Stamm, W.E. 1997. Diagnosis and treatment of uncomplicated urinary
538 tract infection. *Infect. Dis. Clin. North. Am.* **11**, 551-581.
539 Lavelle, J.P., Apodaca, G., Meyers, S.A., Ruiz, W.G., and Zeidel, M.L. 1998. Disruption of
540 guinea pig urinary bladder permeability barrier in noninfectious cystitis. *Am. J. Physiol.* **274**,
541 F205-214.
542 Liang, F., Kachar, B., Ding, M., Zhai, Z., Wu, X.R., and Sun, T.T. 1999. Urothelial hinge as
543 a highly specialized membrane: detergent-insolubility, urohingin association, and in vitro
544 formation. *Differentiation.* **65**, 59-69.
545 Pellecchia, M., Sebbel, P., Hermanns, U., Wüthrich, K., and Glockshuber, R. 1999. Pilus
546 chaperone FimC-adhesin FimH interactions mapped by TROSY-NMR. *Nat. Struct. Biol.* **6**,
547 336-339.
548 Hu, P., Deng, F.M., Liang, F.X., Hu, C.M., Auerbach, A.B., Shapiro, E., Wu, X.R., Kachar,
549 B., and Sun, T.T. 2000. Ablation of uroplakin III gene results in small urothelial plaques,
550 urothelial leakage, and vesicoureteral reflux. *J. Cell. Biol.* **151**, 961-972.
551 Deng, F.M., Ding, M., Lavker, R.M., and Sun, T.T. 2001. Urothelial function reconsidered: a
552 new role in urinary protein secretion. *Urology.* **57**, 117.

553 Grassme, H., Jekle, A., Riehle, A., Schwarz, H., Berger, J., Sandhoff, K., Kolesnick, R., and
554 Gulbins, E. 2001. CD95 signaling via ceramide-rich membrane rafts. *J. Biol. Chem.* **276**,
555 20589-20596.
556 Grassme, H., Schwarz, H., and Gulbins, E. 2001. Molecular mechanisms of ceramide-
557 mediated CD95 clustering. *Biochem. Biophys. Res. Commun.* **284**, 1016-1030.
558 Liang, F.X., Riedel, I., Deng, F.M., Zhou, G., Xu, C., Wu, X.R., Kong, X.P., Moll, R., and
559 Sun, T.T. 2001. Organization of uroplakin subunits: transmembrane topology, pair formation
560 and plaque composition. *Biochem. J.* **355**, 13-18.
561 Ulmschneider, M.B., and Sansom, M.S. 2001. Amino acid distributions in integral membrane
562 protein structures. *Biochim. Biophys. Acta.* **1512**, 1-14.
563 Zhou, G., Mo, W.J., Sebbel, P., Min, G., Neubert, T.A., Glockshuber, R., Wu, X.R., Sun,
564 T.T., and Kong, X.P. 2001. Uroplakin Ia is the urothelial receptor for uropathogenic
565 Escherichia coli: evidence from in vitro FimH binding. *J. Cell. Sci.* **114**, 4095-4103.
566 Hu, P., Meyers, S., Liang, F.X., Deng, F.M., Kachar, B., Zeidel, M.L., and Sun, T.T. 2002.
567 Role of membrane proteins in permeability barrier function: uroplakin ablation elevates
568 urothelial permeability. *Am. J. Physiol. Renal. Physiol.* **283**, F1200-1207.
569 Min, G., Stolz, M., Zhou, G., Liang, F., Sebbel, P., Stoffler, D., Glockshuber, R., Sun, T.T.,
570 Aebi, U., and Kong, X.P. 2002. Localization of uroplakin Ia, the urothelial receptor for
571 bacterial adhesin FimH, on the six inner domains of the 16 nm urothelial plaque particle. *J.*
572 *Mol. Biol.* **317**, 697-706.
573 Simons, K., and Ehehalt, R. 2002. Cholesterol, lipid rafts, and disease. *J. Clin. Invest.* **110**,
574 597-603.
575 Tu, L., Sun, T.T., and Kreibich, G. 2002. Specific heterodimer formation is a prerequisite for
576 uroplakins to exit from the endoplasmic reticulum. *Mol. Biol. Cell.* **13**, 4221-4230.
577 Min, G., Zhou, G., Schapira, M., Sun, T.T., and Kong, X.P. 2003. Structural basis of

578 urothelial permeability barrier function as revealed by Cryo-EM studies of the 16 nm
579 uroplakin particle. *J. Cell. Sci.* **116**, 4087-4094.
580 Apodaca, G. 2004. The uroepithelium: not just a passive barrier. *Traffic.* **5**, 117-128.
581 Los, D.A., and Murata, N. 2004. Membrane fluidity and its roles in the perception of
582 environmental signals. *Biochim. Biophys. Acta.* **1666**, 142-157.
583 Pettersen, E.F., Goddard, T.D., Huang, C.C., Couch, G.S., Greenblatt, D.M., Meng, E.C., and
584 Ferrin, T.E. 2004. UCSF Chimera--a visualization system for exploratory research and
585 analysis. *J. Comput. Chem.* **25**, 1605-1612.
586 Balogh, G., Horváth, I., Nagy, E., Hoyk, Z., Benkö, S., Bensaude, O., and Vígh, L. 2005. The
587 hyperfluidization of mammalian cell membranes acts as a signal to initiate the heat shock
588 protein response. *FEBS. J.* **272**, 6077-6086.
589 Hu, C.C., Liang, F.X., Zhou, G., Tu, L., Tang, C.H., Zhou, J., Kreibich, G., and Sun, T.T.
590 2005. Assembly of urothelial plaques: tetraspanin function in membrane protein trafficking.
591 *Mol. Biol. Cell.* **16**, 3937-3950.
592 Mastronarde, D.N. 2005. Automated electron microscope tomography using robust prediction
593 of specimen movements. *J. Struct. Biol.* **152**, 36-51.
594 Gensure, R.H., Zeidel, M.L., and Hill, W.G. 2006. Lipid raft components cholesterol and
595 sphingomyelin increase H+/OH- permeability of phosphatidylcholine membranes. *Biochem.*
596 *J.* **398**, 485-495.
597 Min, G., Wang, H., Sun, T.T., and Kong, X.P. 2006. Structural basis for tetraspanin functions
598 as revealed by the cryo-EM structure of uroplakin complexes at 6-A resolution. *J. Cell. Biol.*
599 **173**, 975-983.
600 Nicastro, D., Schwartz, C., Pierson, J., Gaudette, R., Porter, M.E., and McIntosh, J.R. 2006.
601 The molecular architecture of axonemes revealed by cryoelectron tomography. *Science.* **313**,
602 944-948.

603 Xie, B., Zhou, G., Chan, S.Y., Shapiro, E., Kong, X.P., Wu, X.R., Sun, T.T., and Costello,
604 C.E. 2006. Distinct glycan structures of uroplakins Ia and Ib: structural basis for the selective
605 binding of FimH adhesin to uroplakin Ia. *J. Biol. Chem.* **281**, 14644-14653.
606 Jenkins, D., and Woolf, A.S. 2007. Uroplakins: new molecular players in the biology of
607 urinary tract malformations. *Kidney. Int.* **71**, 195-200.
608 Khandelwal, P., Abraham, S.N., and Apodaca, G. 2009. Cell biology and physiology of the
609 uroepithelium. *Am. J. Physiol. Renal. Physiol.* **297**, F1477-1501.
610 Thumbikat, P., Berry, R.E., Zhou, G., Billips, B.K., Yaggie, R.E., Zaichuk, T., Sun, T.T.,
611 Schaeffer, A.J., and Klumpp, D.J. 2009. Bacteria-induced uroplakin signaling mediates
612 bladder response to infection. *PLoS. Pathog.* **5**, e1000415.
613 Wang, H., Min, G., Glockshuber, R., Sun, T.T., and Kong, X.P. 2009. Uropathogenic E. coli
614 adhesin-induced host cell receptor conformational changes: implications in transmembrane
615 signaling transduction. *J. Mol. Biol.* **392**, 352-361.
616 Wu, X.R., Kong, X.P., Pellicer, A., Kreibich, G., and Sun, T.T. 2009. Uroplakins in urothelial
617 biology, function, and disease. *Kidney. Int.* **75**, 1153-1165.
618 Emsley, P., Lohkamp, B., Scott, W.G., and Cowtan, K. 2010. Features and development of
619 Coot. *Acta. Crystallogr. D. Biol. Crystallogr.* **66**, 486-501.
620 Kwon, D.N., Park, M.R., Park, J.Y., Cho, S.G., Park, C., Oh, J.W., Song, H., Kim, J.H., and
621 Kim, J.H. 2011. Characterization of a putative cis-regulatory element that controls
622 transcriptional activity of the pig uroplakin II gene promoter. *Biochem. Biophys. Res.*
623 *Commun.* **410**, 264-269.
624 Lee, G. 2011. Uroplakins in the lower urinary tract. *Int. Neurourol. J.* **15**, 4-12.
625 Kanik-Prastowska, I., Lis, J., and Matejuk, A. 2014. Glycosylation of uroplakins.
626 Implications for bladder physiopathology. *Glycoconj. J.* **31**, 623-636.
627 Lee, J.H., de, Val N., Lyumkis, D., and Ward, A.B. 2015. Model Building and Refinement of

628 a Natively Glycosylated HIV-1 Env Protein by High-Resolution Cryoelectron Microscopy.
629 *Structure.* **23**, 1943-1951.
630 Liu, S.L., Sheng, R., Jung, J.H., Wang, L., Stec, E., O'Connor, M.J., Song, S., Bikkavilli,
631 R.K., Winn, R.A., Lee, D. et al. 2017. Orthogonal lipid sensors identify transbilayer
632 asymmetry of plasma membrane cholesterol. *Nat. Chem. Biol.* **13**, 268-274.
633 Min, G., Stolz, M., Zhou, G., Liang, F., Sebbel, P., Stoffler, D., Glockshuber, R., Sun, T.T.,
634 Aebi, U., and Kong, X.P. 2002. Localization of uroplakin Ia, the urothelial receptor for
635 bacterial adhesin FimH, on the six inner domains of the 16 nm urothelial plaque particle. *J.*
636 *Mol. Biol.* **317**, 697-706.
637 Sodt, A.J., Pastor, R.W., and Lyman, E. 2015. Hexagonal Substructure and Hydrogen
638 Bonding in Liquid-Ordered Phases Containing Palmitoyl Sphingomyelin. *Biophys. J.* **109**,
639 948-955.
640 Sorzano, C.O., Alcorlo, M., de, la Rosa- Trevín, J.M., Melero, R., Foche, I., Zaldívar-Peraza,
641 A., del, Cano L., Vargas, J., Abrishami, V., Otón, J. et al. 2015. Cryo-EM and the elucidation
642 of new macromolecular structures: Random Conical Tilt revisited. *Sci. Rep.* **5**, 14290.
643 Sauer, M.M., Jakob, R.P., Eras, J., Baday, S., Eriş, D, Navarra, G., Bernèche, S., Ernst, B.,
644 Maier, T., and Glockshuber, R. 2016. Catch-bond mechanism of the bacterial adhesin FimH.
645 *Nat. Commun.* **7**, 10738.
646 Hagen, W.J.H., Wan, W., and Briggs, J.A.G. 2017. Implementation of a cryo-electron
647 tomography tilt-scheme optimized for high resolution subtomogram averaging. *J. Struct.*
648 *Biol.* **197**, 191-198.
649 Punjani, A., Rubinstein, J.L., Fleet, D.J., and Brubaker, M.A. 2017. cryoSPARC: algorithms
650 for rapid unsupervised cryo-EM structure determination. *Nat. Methods.* **14**, 290-296.
651 Visnjar, T., Chesi, G., Iacobacci, S., Polishchuk, E., Resnik, N., Robenek, H., Kreft, M.,
652 Romih, R., Polishchuk, R., and Kreft, M.E. 2017. Uroplakin traffic through the Golgi

653 apparatus induces its fragmentation: new insights from novel in vitro models. *Sci. Rep.* **7**,
654 12842.
655 Afonine, P.V., Poon, B.K., Read, R.J., Sobolev, O.V., Terwilliger, T.C., Urzhumtsev, A., and
656 Adams, P.D. 2018. Real-space refinement in PHENIX for cryo-EM and crystallography.
657 *Acta. Crystallogr. D. Struct. Biol.* **74**, 531-544.
658 Croll, T.I. 2018. ISOLDE: a physically realistic environment for model building into low-
659 resolution electron-density maps. *Acta. Crystallogr. D. Struct. Biol.* **74**, 519-530.
660 Desai, A.J., and Miller, L.J. 2018. Changes in the plasma membrane in metabolic disease:
661 impact of the membrane environment on G protein-coupled receptor structure and function.
662 *Br. J. Pharmacol.* **175**, 4009-4025.
663 Emsley, P., and Crispin, M. 2018. Structural analysis of glycoproteins: building N-linked
664 glycans with Coot. *Acta. Crystallogr. D. Struct. Biol.* **74**, 256-263.
665 Goddard, T.D., Huang, C.C., Meng, E.C., Pettersen, E.F., Couch, G.S., Morris, J.H., and
666 Ferrin, T.E. 2018. UCSF ChimeraX: Meeting modern challenges in visualization and
667 analysis. *Protein. Sci.* **27**, 14-25.
668 Ghysels, A., Krämer, A., Venable, R.M., Teague, W.E. Jr, Lyman, E., Gawrisch, K., and
669 Pastor, R.W. 2019. Permeability of membranes in the liquid ordered and liquid disordered
670 phases. *Nat. Commun.* **10**, 5616.
671 Liebschner, D., Afonine, P.V., Baker, M.L., Bunkóczi, G., Chen, V.B., Croll, T.I., Hintze, B.,
672 Hung, L.W., Jain, S., McCoy, A.J. et al. 2019. Macromolecular structure determination using
673 X-rays, neutrons and electrons: recent developments in Phenix. *Acta. Crystallogr. D. Struct.*
674 *Biol.* **75**, 861-877.
675 Righetto, R.D., Biyani, N., Kowal, J., Chami, M., and Stahlberg, H. 2019. Retrieving high-
676 resolution information from disordered 2D crystals by single-particle cryo-EM. *Nat.*
677 *Commun.* **10**, 1722.

678 Kusumi, A., Fujiwara, T.K., Tsunoyama, T.A., Kasai, R.S., Liu, A.A., Hirosawa, K.M.,
679 Kinoshita, M., Matsumori, N., Komura, N., Ando, H. et al. 2020. Defining raft domains in the
680 plasma membrane. *Traffic.* **21**, 106-137.
681 Ord, M., Faustova, I., and Loog, M. 2020. The sequence at Spike S1/S2 site enables cleavage
682 by furin and phospho-regulation in SARS-CoV2 but not in SARS-CoV1 or MERS-CoV. *Sci.*
683 *Rep.* **10**, 16944.
684 Tsugawa, H., Ikeda, K., Takahashi, M., Satoh, A., Mori, Y., Uchino, H., Okahashi, N.,
685 Yamada, Y., Tada, I., Bonini, P. et al. 2020. A lipidome atlas in MS-DIAL 4. *Nat.*
686 *Biotechnol.* **38**, 1159-1163.
687 Johnson, B.A., Xie, X., Bailey, A.L., Kalveram, B., Lokugamage, K.G., Muruato, A., Zou, J.,
688 Zhang, X., Juelich, T., Smith, J.K. et al. 2021. Loss of furin cleavage site attenuates SARS-
689 CoV-2 pathogenesis. *Nature.* **591**, 293-299.
690 Jumper, J., Evans, R., Pritzel, A., Green, T., Figurnov, M., Ronneberger, O.,
691 Tunyasuvunakool, K., Bates, R., Žídek, A., Potapenko, A. et al. 2021. Highly accurate
692 protein structure prediction with AlphaFold. *Nature.* **596**, 583-589.
693 Pettersen, E.F., Goddard, T.D., Huang, C.C., Meng, E.C., Couch, G.S., Croll, T.I., Morris,
694 J.H., and Ferrin, T.E. 2021. UCSF ChimeraX: Structure visualization for researchers,
695 educators, and developers. *Protein. Sci.* **30**, 70-82.
696 Prestegard, J.H. 2021. A perspective on the PDB's impact on the field of glycobiology. *J.*
697 *Biol. Chem.* **296**, 100556.
698 Zhang, T., Hu, W., and Chen, W. 2021. Plasma Membrane Integrates Biophysical and
699 Biochemical Regulation to Trigger Immune Receptor Functions. *Front. Immunol.* **12**,
700 613185.
701 Zhao, P., Zhao, C., Chen, D., Yun, C., Li, H., and Bai, L. 2021. Structure and activation
702 mechanism of the hexameric plasma membrane H(+)-ATPase. *Nat. Commun.* **12**, 6439.

El, Mazouni D., and Gros, P. 2022. Cryo-EM structures of peripherin-2 and ROM1 suggest multiple roles in photoreceptor membrane morphogenesis. *Sci. Adv.* **8**, eadd3677.

Evans, R., O'Neill, M., Pritzel, A., Antropova, N., Senior, A., Green, T., Zidek, A., Bates, R., Blackwell, S., Yim, J. et al. 2022. Protein complex prediction with AlphaFold-Multimer. *bioRxiv.* **DOI**, 10.1101/2021.10.04.463034.

Mirdita, M., Schütze, K., Moriwaki, Y., Heo, L., Ovchinnikov, S., and Steinegger, M. 2022. ColabFold: making protein folding accessible to all. *Nat. Methods.* **19**, 679-682.

Oda, T., Yanagisawa, H., Shinmori, H., Ogawa, Y., and Kawamura, T. 2022. Cryo-electron tomography of Birbeck granules reveals the molecular mechanism of langerin lattice formation. *Elife.* **11***:* e79990.

Watanabe, T., Suzuki, A., Ohira, S., Go, S., Ishizuka, Y., Moriya, T., Miyaji, Y., Nakatsuka, T., Hirata, K., Nagai, A. et al. 2022. The Urinary Bladder is Rich in Glycosphingolipids Composed of Phytoceramides. *J. Lipid. Res.* **63**, 100303.

Dutka, P., Metskas, L.A., Hurt, R.C., Chou, T., Shapiro, M.G., and Jensen, G.J. 2023. Structure of Anabaena flos-aquae gas vesicles revealed by cryo-ET. *Biophys. J.* **122**, 40A.